Radio diagnosis of coronal magnetic field, non-thermal electrons, and fine structures associated with microwave bursts

Huang Guangli *
Purple Mountain Observatory, Chinese Academy of Science, Nanjing, China
glhuang@pmo.ac.cn

Abstract

Key words: magnetic field — non-thermal electrons — magnetic reconnection — microwave bursts

1. Introduction

It is necessary to solve two key problems before any models of solar flares or coronal mass ejections (CMEs) are well compared with solar observations (Forbes, 2004).

1. How to measure coronal magnetic field and to get the favor magnetic configuration in corona, where flares and CMEs are triggered by magnetic reconnections.

2. How to determine the exact time and location of magnetic reconnections if the scale of current sheets are much smaller than the spatial resolution of present solar telescopes.

It is well known that radio observations under different radiation mechanisms may provide a unique diagnosis of coronal magnetic field and the non-thermal electrons. Some techniques for radio measurements of the magnetic fields in both chromosphere and corona were reviewed by Kundu (1990), such as the measurement of polarization at millimeter bands for estimating the magnetic field in the active regions of chromosphere, the properties of gyroresonance radiation in microwaves for estimating the magnetic field in corona above the active regions, and a direct measurement of the coronal magnetic field using cyclotron line emission. The author of this paper will pay attention only to the radio diagnosis of coronal magnetic field and non-thermal electrons associated with microwave bursts, which means the radiation mechanism in this case is dominated by the non-thermal gyro-synchrotron emissions and relevant absorptions.

On the other hand, the fine structures (FS) at decimeter and centimeter bands have been intensively studied with observations of the radio dynamic spectra in recent solar circles. It is believed that these FS may be considered as the radio signatures of magnetic reconnections and particle acceleration. For example, the start frequencies of type *III* bursts are emitted at the level in corona where non-thermal electrons are accelerated. The radio millisecond spikes may be more closed to the acceleration site than type *III* bursts (Benz et al., 1982). Especially, the bidirectional frequency drifts caused by the electron beams accelerated from reconnection site in two opposite directions may show the level of reconnection site in corona at the reversal frequencies (Robison et al. 2000; Xie et al. 2000; Huang et al. 1998, 2004a). Moreover, type *II* or *IV* bursts and relevant FS (such as zebra strips) are closely associated with shock waves and CMEs (Mclean, 1985), their start frequencies correspond to the level in corona where the speed of CMEs is larger than the local Alfvén speed.

The time and frequency resolutions become as high as possible in some recent solar radio spectrographs for observing the FS. But it is difficult to locate the compact sources of these FS in solar disk for understanding their relationship with the other solar resolvable observations. Before some new radio telescopes with high spatial, temporal, and frequency resolutions (such as FASR) are completed in near future, it is considerable to use the radio data with spatial resolutions, such as the Nobeyama Radio Heliograph (NoRH) and etc, together with the data of radio spectrographs for the researches on the radio diagnosis of coronal magnetic field, non-thermal electrons, and fine structures associated with microwave bursts. Some recent works are reviewed in this paper.

2. Diagnosis of coronal magnetic field and non-thermal electrons

2.1. Approximations used by Dulk & Marsh

Dulk & Marsh (1982) managed to simplify generally the complicated expressions for gyro-synchrotron emissions (Krüger, 1979) in a series of exponential forms that can be related to observations, but that the magnetic field, the density of non-thermal electrons, and the propagation angle are given in an implicit, and thus not practical form. Based on the approximation used in Dulk & Marsh (1982), the explicit expressions of the coronal magnetic field and the line-of-sight number of non-thermal electrons versus brightness temperature, frequency, turnover frequency, and spectral index were proposed by Zhou & Karlický (1994) and Huang & Zhou (1999) for solar microwave bursts with non-thermal gyro-synchrotron radiation mechanism.

$$B = \left[\frac{c^2}{k_B T_{b\nu} A_1}\nu_p^{1.3+0.98\delta}\nu^{-0.78-0.9\delta}\right]^{\frac{1}{0.52+0.08\delta}} \quad (1)$$

* The author would like to thank the SOC of Nobeyama Symposium, 2004 for the review paper in the Proceedings. This study is supported by the NFSC projects No.10333030 and 10273025, and "973" program with No.G2000078403.

$$A_1 = 4.24\times10^{14+0.3\delta}(\sin\theta)^{0.34+0.07\delta}\times$$
$$\times(2.8\times10^6)^{2.52+0.08\delta} \quad (2)$$

$$NL = T_{b\nu}\Big(\frac{k_B\nu^2}{c^2}\Big)A_2^{-1}B^{-1} \quad (3)$$

$$A_2 = 3.3\times10^{-24-0.52\delta}(\sin\theta)^{-0.43+0.65\delta}\Big(\frac{\nu}{\nu_B}\Big)^{1.22-0.9\delta} \quad (4)$$

Here, B is the magnetic field strength. c is the velocity of light in vacuum. k_B is the Boltzmann constant. $T_{b\nu}$ and S_ν are respectively the brightness temperature and the radio flux at a given frequency ν in the optical thin part of the microwave spectra. ν_p is the peak or the turnover frequency. ν_B is the electron gyro-frequency. θ refers to the angle between wave vector and magnetic field. δ is the energetic spectral index of non-thermal electrons with a single power law distribution, and $\delta = (1.22-\gamma)/0.9$, γ is the radiation spectral index (Dulk & Marsh, 1982).

However, the propagation angle θ is still remained as a free or unmeasurable parameter in these expressions. Hence, the coronal magnetic field and the density of non-thermal electrons can not be calculated self-consistently using Eqs.(1)-(4). One method was proposed by Huang & Nakajima (2002) to solve the propagational angle with the polarization degree r_c (Dulk, 1985), together with brightness temperature, frequency, turnover frequency, and spectral index.

$$r_c = 1.26\times10^{0.035\delta}10^{-0.071\cos\theta}\Big(\frac{\nu}{\nu_B}\Big)^{-0.782+0.545\cos\theta} \quad (5)$$

which is rewritten as an equation of x ($x=\sin\theta$):

$$x^2 + \left(\frac{c_2+c_3\log_{10}x}{c_4+c_5\log_{10}x}\right)^2 = 1 \quad (6)$$

All of the coefficient in Eq. (6) are measurable and defined in Huang & Nakajima (2002). After the angle is solved from Eq. (6), the 2-dimensional distribution of the coronal magnetic field strength is calculated self-consistently in one event on Nov. 28, 1998 observed by NoRH. Fig.1 shows the contours (100-600 Gauss) of the calculated magnetic field strength overlaid on the brightness temperature of NoRH at 17 GHz in different times of the microwave burst. In fact, two components of magnetic field parallel and perpendicular to the wave vector are obtained in these calculations with the solved propagational angles.

Another way to solve the angle was obtained by Huang (2004b) with the expression of the turnover frequency in Dulk (1985).

$$\nu_p \approx 2.72\times10^{3+0.27\delta}(\sin\theta)^{0.41+0.03\delta}(NL)^{0.32-0.03\delta}$$
$$\times B^{0.68+0.03\delta} \quad (7)$$

the logarithm of Eqs.(1), (3) and (7) will lead to three linear equations of B, NL, and θ, which are readily solved to get three explicit expressions of B, NL, and θ versus ν, $T_{b\nu}$, δ, and ν_p as shown in Eqs.(8)-(10) (Huang, 2004b):

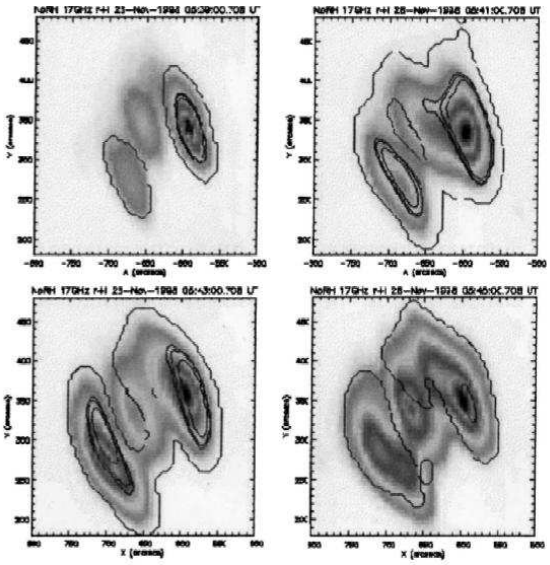

Fig. 1. The contours (100-600 Gauss) of the calculated magnetic field strength overlaid on the brightness temperature of NoRH at 17 GHz in different times of a microwave burst on Nov. 28, 1998.

$$\sin\theta = 10^{f_{11}(\delta)}T_{b\nu}^{f_{12}(\delta)}\nu^{f_{13}(\delta)}\nu_p^{f_{14}(\delta}) \quad (8)$$

$$NL = 10^{f_{21}(\delta)}T_{b\nu}^{f_{22}(\delta)}\nu^{f_{23}(\delta)}\nu_p^{f_{24}(\delta}) \quad (9)$$

$$B = 10^{f_{31}(\delta)}T_{b\nu}^{f_{32}(\delta)}\nu^{f_{33}(\delta)}\nu_p^{f_{34}(\delta}) \quad (10)$$

All of these coefficients are defined as the functions of δ (Huang, 2004b). The general calculations from Eqs.(8)-(10) for the relationship of B versus ν, $T_{b\nu}$, δ, and ν_p are displayed in Fig.2. When $\delta < 3.5$, B is monotonously increasing with ν and $T_{b\nu}$ respectively, and decreasing with ν_p. When $3.5 \le \delta < 6.0$, B is monotonously decreasing with ν and $T_{b\nu}$ respectively, and increasing with ν_p. When $\delta \ge 6.0$, B is again monotonously increasing with ν and $T_{b\nu}$ respectively, and decreasing with ν_p. Hence, B is a non-monotonic function of δ for given ν, ν_p, and $T_{b\nu}$.

On the other hand, the relationship of the line-of-sight number of non-thermal electrons with ν_p, ν, and $T_{b\nu}$ respectively does not change with different values of δ. NL is always monotonously increasing with ν and T_b respectively, and decreasing with ν_p. Hence, NL is a monotonic function of δ, and NL always increases with increasing the value of δ for a given ν, ν_p, and $T_{b\nu}$.

2.2. Ramaty and Takakura's model

It is emphasized that the approximations used by Dulk & Marsh (1982) are only available for $2 < \delta < 7$, $10 < s < 100$ (s is harmonic number), low energy cutoff equals $10keV$, $\theta \sim 20^\circ - 80^\circ$, ν_p defined as the frequency at the optical depth $\tau \approx 1$, and the emission of X-mode. Also, these approximations can be used only for a simple and isolated source without significant changes of the magnetic field, the angle and etc, along the line-of-sight within the emission region.

The more strict model of non-thermal gyro-synchrotron

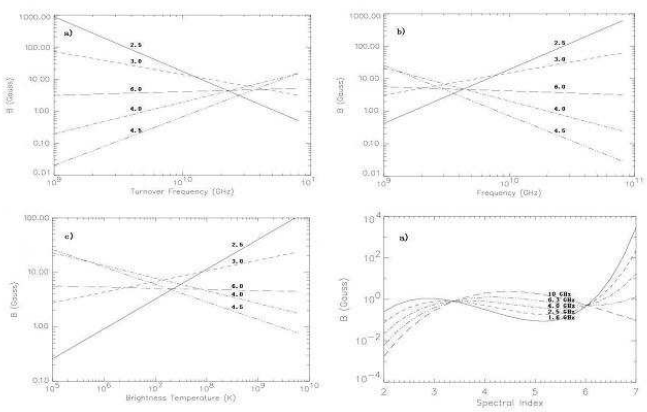

Fig. 2. The calculated magnetic field B versus a. ν_p with ($\nu = 10^{11} Hz$ and $T_{b\nu} = 10^6 K$, b. ν with $T_{b\nu} = 10^6 K$ and $\nu_p = 10^9 Hz$, and c. $T_{b\nu}$ with $\nu = 2.0 \times and 10^9 Hz$, $\nu_p = 10^9 Hz$. The value of δ is selected as 2.5 with solid line, 3.0 with short--dashed line, 4.0 with dot-dashed line, 4.5 with dot-dot-dot–dashed line, and 6.0 with long-dashed line, respectively. The panel d. for the calculated magnetic field B versus the spectral index with $\nu = 10^{10} Hz$, $T_{b\nu} = 10^6 K$, and different values of ν_p from 1.6 GHz to 10.0 GHz.

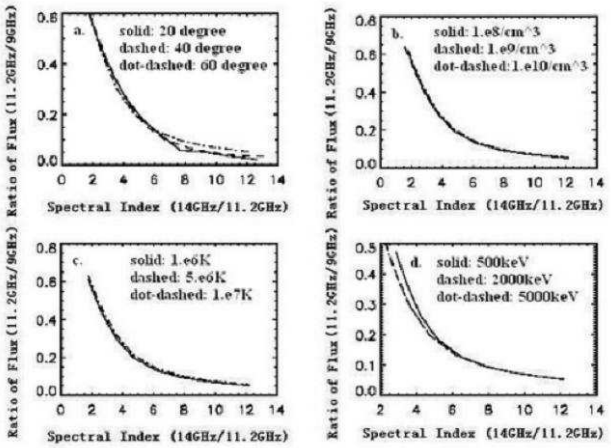

Fig. 3. The effects of different p_{max}, N, T, and θ on the graph of the ratio of flux at 11.2 GHz and 9 GHz versus γ calculated from the ratio of flux at 14 GHz and 11.2 GHz. a. $\theta = 20, 40, 60°$, $N = 10^9 cm^{-3}$, $T = 5 \times 10^6 K$, $E_{max} = 5MeV$, b. $N = 10^8, 10^9, 10^{10} cm^{-3}$, $\theta = 60°$, $T = 5 \times 10^6 K$, $E_{max} = 5MeV$, c. $T = 10^6, 5 \times 10^6, 10^7 K$, $\theta = 60°$, $N = 10^9 cm^{-3}$, $E_{max} = 5MeV$, d. $E_{max} = 0.5MeV, 2MeV, 5MeV$, $\theta = 60°$, $N = 10^9 cm^{-3}$, $T = 5 \times 10^6 K$. Some parameters are fixed, such as B_0=800 Gauss, δ =2-7, $E_{min} = 10keV$ in all panels.

radiations with a single power-law distribution ($F(E) = AE^{-\delta}$) are derived by Ramaty (1969) and Takakura et al. (1970), in which the thermal cyclotron resonant absorption and a dipole magnetic field are considered. The Razin effect and self-absorption may be neglected at higher frequencies or optical-thin part.

$$T_{b\nu_\mp} = \frac{A\pi e^2 cd}{3k_B}(2.8 \times 10^6 B_0)^{1/3} F_{\nu_\mp}, \quad (11)$$

$$F_{\nu_\mp} = \int \eta_{\nu_\mp} s^{-2/3} \exp^{-\sum_{s+1}^{6} \tau_{js}} ds \quad (12)$$

$$\eta_{\nu_\mp} = \frac{1}{2|\cos\theta|} \sum_{n=s+1} \int_{p_{min}}^{p_{max}} (a \pm b)^2 \frac{(\sqrt{1+p^2}-1)^{-\delta}}{1+p^2} dp \quad (13)$$

$$\tau_{js} = \frac{\pi e^2}{m_0 c}(\frac{k_B T}{m_0 c^2})^{s-1} \frac{s^{2s}}{2^s s!} dN\nu(\sin\theta)^{2(s-1)} \times n_\pm \quad (14)$$

$$n_\pm = \frac{(\sin^2\theta + 2s\cos^2\theta \pm \sqrt{\sin^4\theta + 4s^2\cos^2\theta})^2}{\sin^4\theta + 4s^2\cos^2\theta \pm \sin^2\theta\sqrt{\sin^4\theta + 4s^2\cos^2\theta}}. \quad (15)$$

Here, $T_{b\nu_\mp}$, $F_{\nu_\mp}$, and $\eta_{\nu_\mp}$ are respectively brightness temperature, flux, and emissivity at a give frequency ν. The sign of $\mp$ refers to the ordinary or extraordinary modes in the cold plasma dispersion relation. m_0 is the mass of an electron. B_0 is the magnetic field in photosphere. d is the scale of the dipole magnetic field. N and T are respectively the density and the temperature of the ambient plasma. p_{min} and p_{max} are the momentum in respect to E_{min} (low cutoff energy) and E_{max} (high cutoff energy).

There are more free parameters in Eqs.(11)-(15) than that in the approximations used by Dulk and Marsh (1982), such as A, B_0, p_{min}, p_{max}, N, T, and θ. The effects of θ, N, T, and p_{max} on the calculations are shown by the ratio of flux at 11.2 GHz and 9 GHz versus γ calculated from the ratio of flux at 14 GHz and 11.2 GHz, in which $\theta = 20, 40, 60°$, $N = 10^8, 10^9, 10^{10} cm^{-3}$, $T = 10^6, 5 \times 10^6, 10^7 K$, $E_{max} = 0.5MeV, 2MeV, 5MeV$, respectively from left-top to right-bottom panel (Huang, 2004c). The coefficient A of power-law is just cancelled by the ratio between two frequencies. It is evident that the variation of θ, N, T, and p_{max} with typical values ranged in corona only make small difference in the curves of Fig.3.

When the magnetic field B_0 is 200, 500, and 800 Gauss, the calculated curves are separated evidently in Fig.4. Hence, the local magnetic field is a very sensitive parameter to the calculations (Huang, 2004c).

Moreover, the variation of E_{min} from 10-90 keV also has strong effect on the calculations as shown in Fig.5.

Therefore, some insensitive parameters may be fixed, such as θ, N, T, and p_{max}, but the magnetic field and the low energy cutoff have to be solved together. On the other hand, the low energy cutoff is fixed as 10 keV in the approximations used by Dulk & Marsh (1982). So, the calculations of Eqs.(1)-(10) are still not self-consistent. On the other hand, if the range of low energy cutoff is limited in small values such as 10-30 keV (Huang, 2004c), Eqs.(1)-(10) may be a good approximations of magnetic field and non-thermal density.

A more recent calculations with Eqs.(11)-(15) show the density of non-thermal electrons in loop top source is always larger than that in foot point source in two examples of NoRH (Fig.6), in one of which foot points are much strong than loop top, but in another event, the loop top

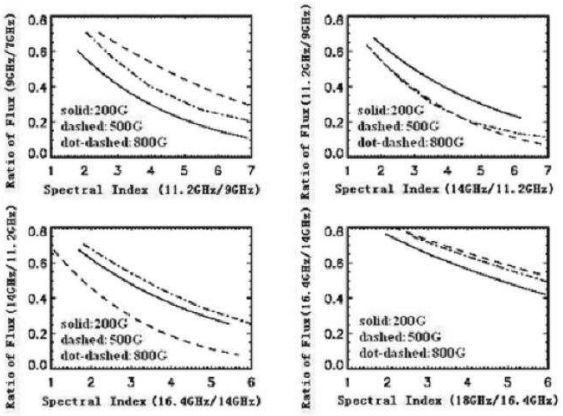

Fig. 4. The magnetic field B_0 is 200 (solid), 500 (dashed), and 800 (dot-dashed) Gauss respectively for different ratio and γ ($(\delta = 5,\ \theta = 60^\circ,\ N = 10^9 cm^{-3},\ T = 5 \times 10^6 K,\ E_{min} = 10keV,\ E_{max} = 5MeV$).

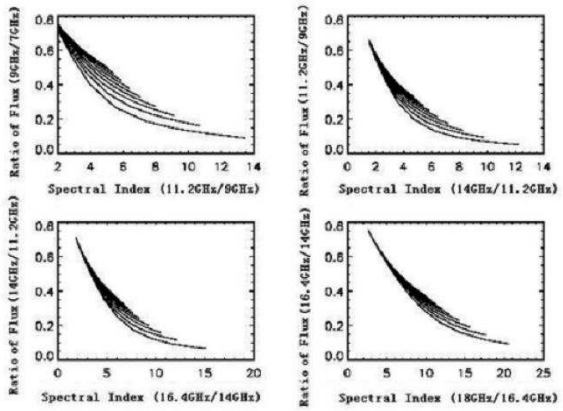

Fig. 5. The magnetic field B_0 is 800 Gauss for different ratio and γ, $E_{min} = 10 - 90keV$, respectively from bottom to top of each panel, $N = 10^9 cm^{-3}$, $T = 5 \times 10^6 K$, $E_{max} = 5MeV$, $\theta = 60^\circ$, $\delta = 2 - 7$.

is much stronger than foot points (Zhou et al., 2004).

3. Diagnosis of the location of radio fine structures

3.1. Millisecond spikes at 2.6-3.8 GHz

Solar radio millisecond spikes are recognized as the solar magnetic activities with the smallest time and space scale, and well associated with HXR elementary bursts, as well as evidence for the coherent plasma emission and particle acceleration with short time scale originated from magnetic reconnections sites or shock fronts. The millisecond spikes are often detected in decimeter bands (Benz, 1986), with time scales of several ten or hundred milliseconds, narrow bandwidth of 2-5 percent, and fast drift rate of several tens to hundreds MHz per second.

It is difficult to locate the sources of spike emissions due to their very compact size (hundreds or even tens km) predicted from the short time scale and narrow bandwidth. Some measurements were reported by Krucker et al. (1995, 1997) with VLA at 333 MHz and YOHKOH/SXT, respectively. A scenario is proposed where the energy is released in or near the spike source, and in which the spikes, the type *III* bursts and the thermal source originate from the same energy release. Another measurement was reported by Altyntsev et al. (1995) with SSRT at 5.7 GHz, the source size is unexpected large (tens arcsec) may be caused by the strong angular scattering at centimeter bands (Bastian, 1994).

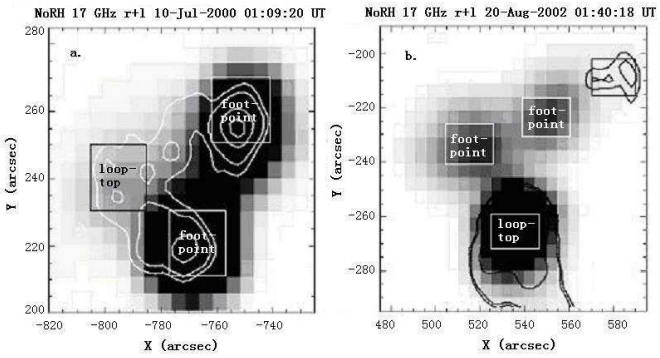

Fig. 6. a. The NoRH image at 17 GHz on July, 10, 2000. b. The NoRH image at 17 GHz on Aug 20, 2002.

One event on Nov.2, 1997 is studied at 2.6-3.8 GHz with high time (8 ms) and frequency (10 MHz) resolutions (Huang, 2004d). Several spikes with lifetime of tens ms and relative bandwidth of 2-3% were superposed on the ambient burst (Fig.7). The most interesting feature of one spike at 03:04:54.6 UT (marked in Fig.7) is a very fast frequency drift (several GHz/s) in bi-direction with reversal frequency at about 3 GHz (Fig.8), which is important to determine the level of magnetic reconnection in corona (Liu et al., 2002).

Figs.9-10 show the NoRH contours at 17 GHz overlaid on YOHKOH/SXT and SOHO/MDI images around the time of spike emissions. The radio source is composed of one extended source is embedded in a large and bright soft X-ray loop system, and a compact source located at one foot-point of a small soft X-ray loop. The magnetic field is simplified as a dipole with multiple positive (white) and negative (black) polarities. The 17 GHz contours are marked by "a" (compact source), and "b, c, d, e, f" (extended source). Fig.11 show the time profiles at these sub-sources, the counterpart of the radio spike at 03:04:54.6 UT only exists in the compact source, with Stocks I, V components and polarization degree in Fig.12. Moreover, the magnetic field in the compact source is larger than that in the extended source, the condition the electron cyclotron maser mechanism for spike emissions is satisfied only in the compact source, i.e., the electron plasma frequency is smaller than the electron gyrofrequency (Huang, 1987).

Even the working frequencies of NoRH is much larger

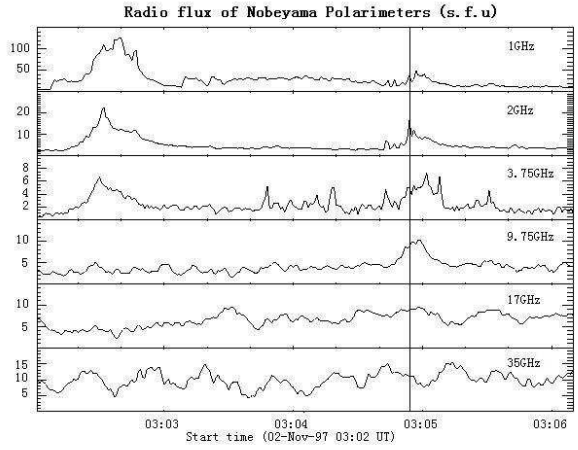

Fig. 7. The time profiles at 1, 2, 3.75, 9.75, 17, and 35 GHz of NoRP on Nov.2, 1997. The line is marked as the selected time of a radio spike.

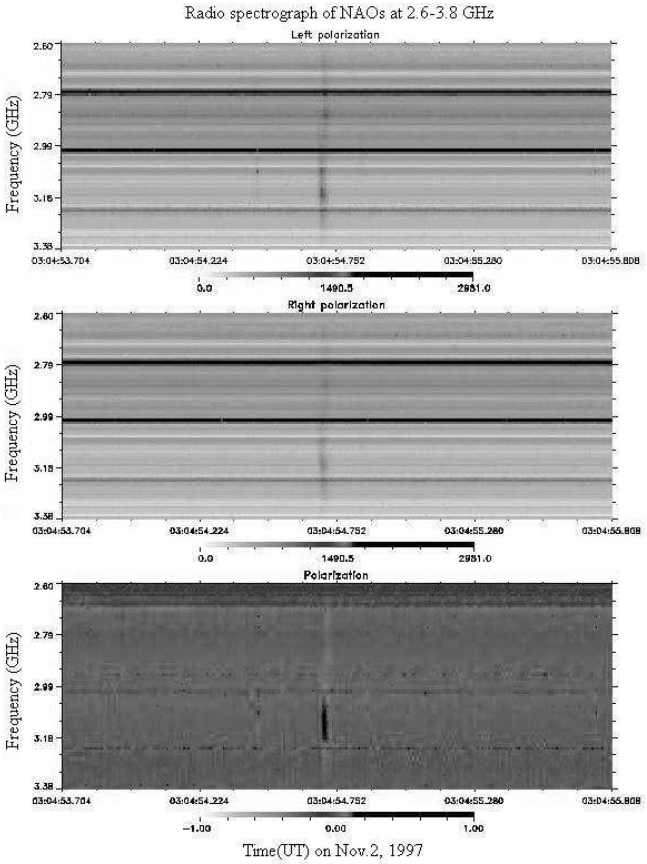

Fig. 8. The 2.6-3.8 dynamic spectrum of a radio spike at 03:04:54.6 UT on Nov.2, 1997.

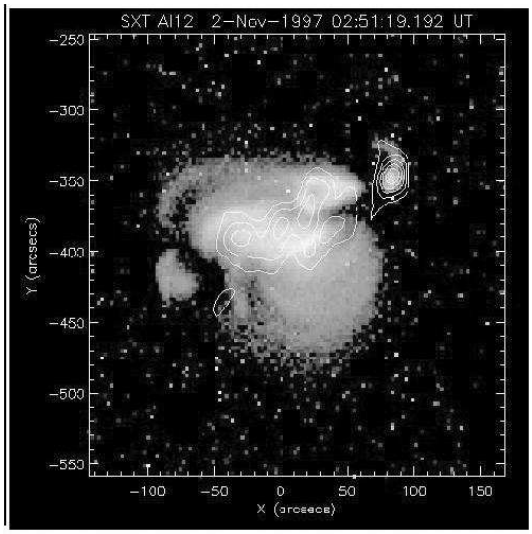

Fig. 9. The contour of the radio source at NORH 17 GHz (03:04:58 UT) overlapped on the YOHKOH/SXT (03:15:04.135 UT) image in AR8100 on Nov. 2, 1997.

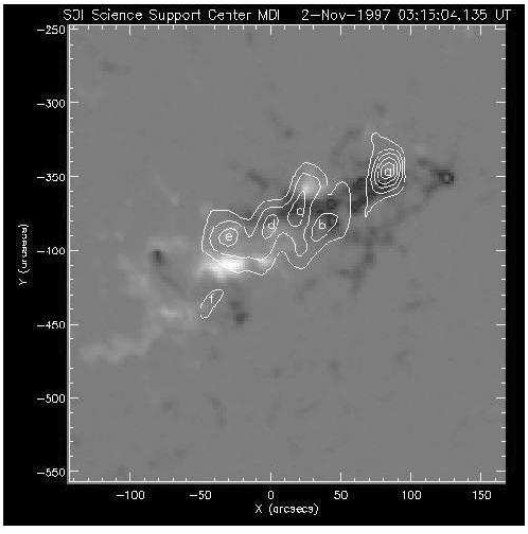

Fig. 10. The contour of the radio source at NoRH 17 GHz (03:04:58 UT) overlapped on SOHO MDI magnetogram at 03:15:04135 UT on Nov. 2, 1997.

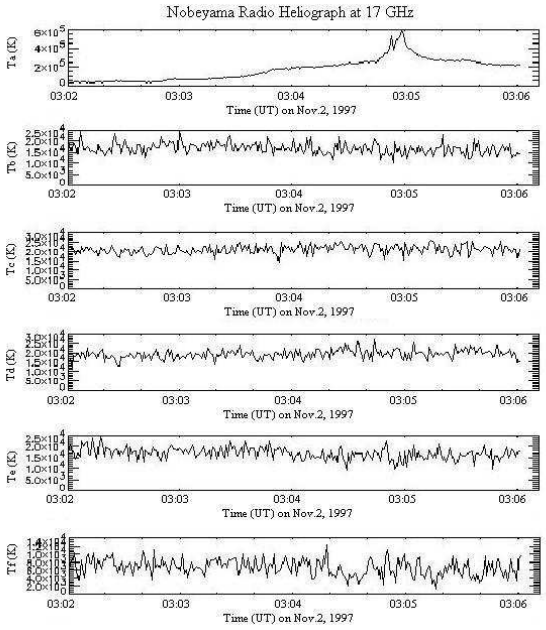

Fig. 11. The time profile of NoRH 17 GHz in the marked positions "a-f" as in Fig.6.

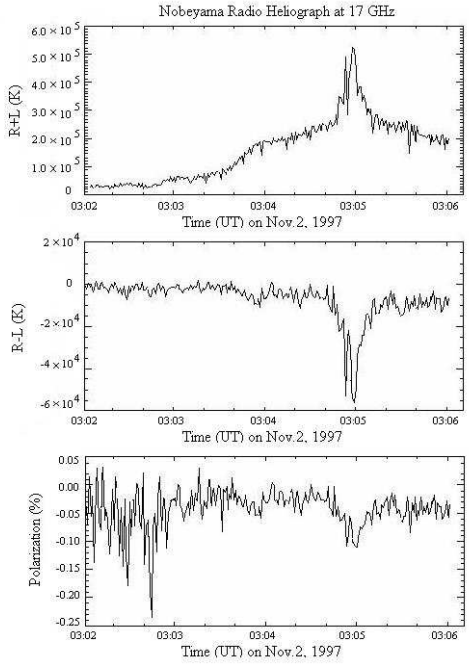

Fig. 12. The I (R+L), V (R-L) components and polarization of NoRH 17 GHZ in the compact source on Nov. 2, 1997.

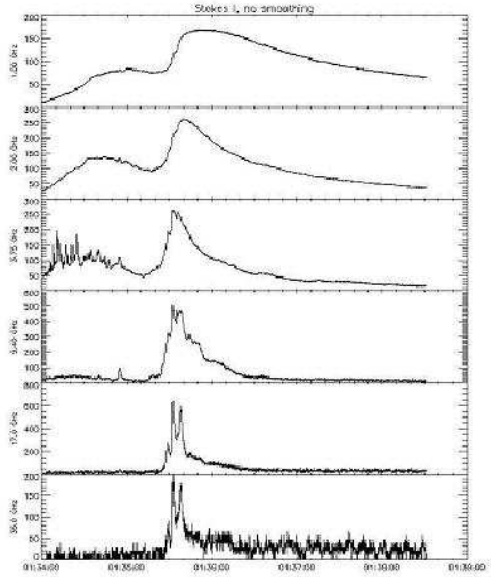

Fig. 13. The time profiles at 1, 2, 3.75, 9.75, 17, and 35 GHz of NoRP on Aug.25, 1999.

than that of the spectrograph, and the counterpart of the spike at 17 GHz is not clear in NoRP data (Fig.7), but it is really visible in NoRH data with high spatial resolution and sensitivity. The physical explanation for this counterpart is that the electron beams for spike emissions at lower frequencies may reach very low corona for 17 GHz emissions.

3.2. Type III-like at 4.5-7.5 GHz

Fig.13 gives another example of rich fine structures (FS) started about one minute prior to the main burst with the maximum emission at 4 GHz for the FS, and 10 GHz for the main burst, respectively. The time profiles at 4.5-7.5 GHz coincide very well with that of hard X-ray (from 25 keV to >300 keV) in both of the main burst and the FS as shown in Fig.14 (Huang et al., 2003).

The dynamic spectrum at 4.5-7.5 GHz in the top panel of Fig.14 show a group of type *III*-like bursts with drifts from lower to higher frequencies, which means that the electron beams move down from higher to lower corona. The burst at the start frequency around 4 GHz should be emitted close to the level of acceleration or reconnection site. The sources of the FS and main burst are located in Fig.15, the double source appeared, and down source (FS) was only strong in the pre-flare phase, after that the up source (main burst) was dominated. The SOHO/MDI contours in Fig.16 shows a typical dipole magnetic field around the main source, which should be contributed by the foot-point emissions. On the other hand, the FS seem to be emitted close to the loop top, which is consistent with the typical flare model. The location of FS is confirmed by the time profiles of different sources. Fig.17 gives the Stocks I and V at 17 GHz of the main and FS sources. It is evident that a strong fluctuations in the pre-

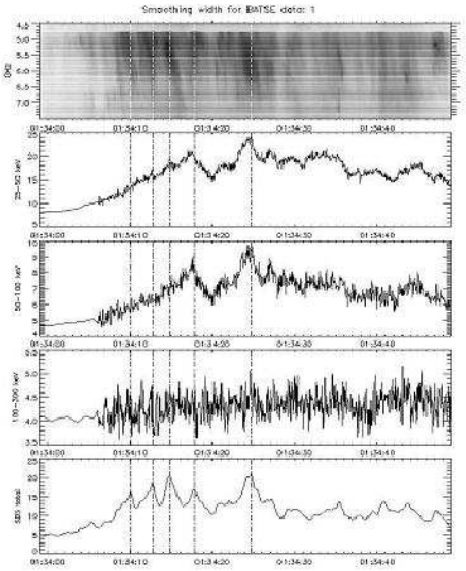

Fig. 14. The comparison between the time profiles of BATSE X-ray (three middle panels for three energy channels) and the spectrum of radio FS at 4.5-7.5 GHz (top panel) as well as the integrated time profile in full band (bottom panel) on Aug 25, 1999.

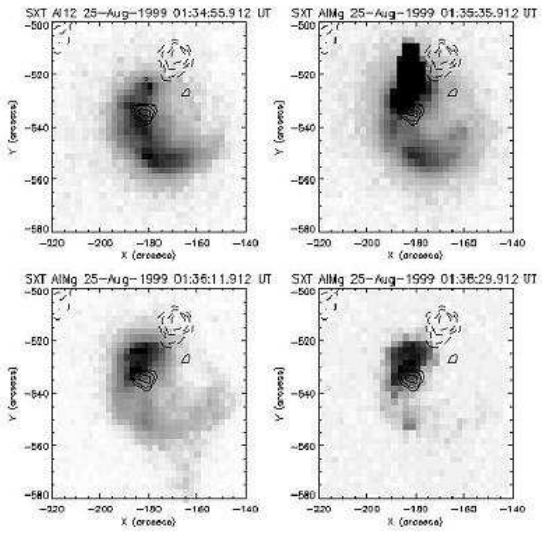

Fig. 16. The contours of SOHO/MDI (solid lines for 200 G, 300 G, and 400 G, dashed lines from -200 G to -1000 G with interval of 200 G) overlaid on YOHKOH/SXT images in the event on Aug 25, 1999.

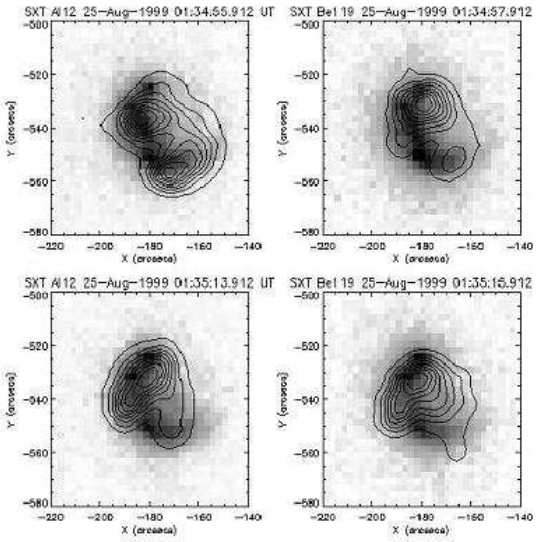

Fig. 15. The contours of R+L at 17 GHz of NoRH (5×10^4-10^6 K) overlaid on YOHKOH/SXT images in the pre-flare and rising phases of the event on Aug 25, 1999.

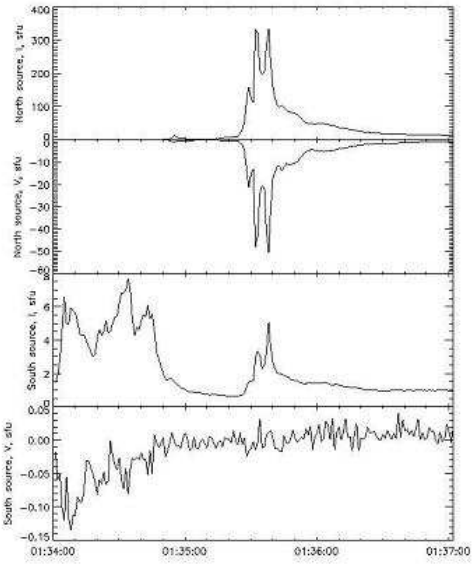

Fig. 17. The time profiles (Stokes I) and polarization (Stokes V) at 17 GHz of NoRH in the main (first and second panels) and FS (third and fourth panels) sources, respectively.

flare phase only happened in the source of FS at 17 GHz, which is consistent with the time profile at 3.75 GHz in Fig.13.

The dynamic spectrum with high time resolution (5 ms) in Fig.18 shows one example of the type *III*-like, which may be considered as a twisted magnetic rope with time

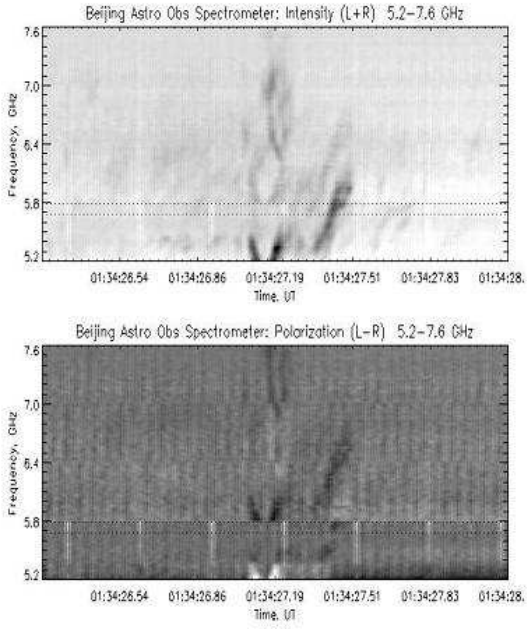

Fig. 18. The dynamic spectrum with time resolution of 5ms for a selected type *III*-like at 5.2-7.6 GHz of NAO on Aug 25, 1999.

interval of 0.3 s and frequency interval of 0.5 GHz, and the phase velocity of a typical Alfvén speed (Huang et al., 2003).

3.3. Microwave type IV and III, and zebra at 2.6-7.6 GHz

In an event on April 21, 2002 with X1.5 flare and very high-speed CME (Huang, 2004e), the time evolution of TRACE images overlaid by NoRH 17 GHz contours (Fig.19). The main radio burst started at higher frequencies as shown in the first panel with a double source at two foot-points as shown in SOHO/MDI magnetograph and 34 GHz contours of NoRH (Fig.20). After that, a radio ejection was detected from foot 1 at 01:49 UT (while foot 2 disappeared), associated with the expanded flare and post-flare loops. The loop-top was extended along the solar limb and well coincident with the EUV loops. The velocity of radio ejection and expanded loops keeps ten km/s until the post-flare phase.

It is emphasized that the polarization sense of the radio ejection at loop-top source (LCP) is opposite to that at foot 1 (RCP) as shown in Fig.21.

Figs.22-23 show the Stokes I and V profiles at 1, 2, 3.75, 9.75, 17 and 35 GHz of NoRP in this event. The maximum time is around 01:25 UT with turnover frequency of about 10 GHz corresponding to the 17 GHz emission from foot 2 source in Figs.19-20. Almost during the same time as the radio ejection started (01:50 UT) from foot 1, a very strong emission at low frequencies (1-2 GHz) appeared with reversal polarization sense from RCP to LCP, which predicted as the coherent emissions by Kundu et al. (2004).

The coherent emissions are analyzed with dynamic

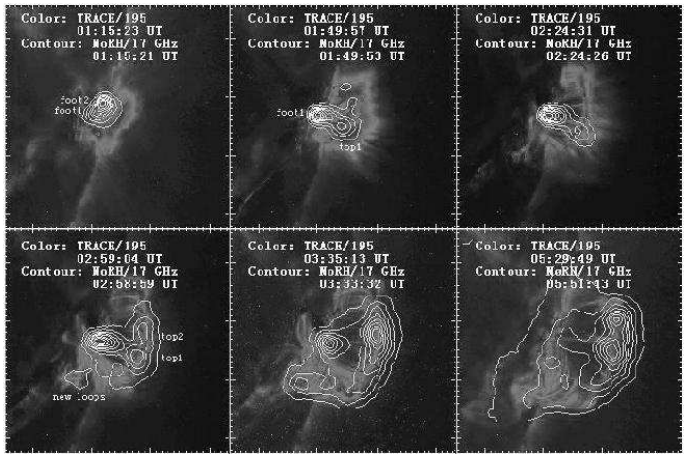

Fig. 19. The TRACE images overlaid by 17 GHz contours of NoRH at different phase of the event

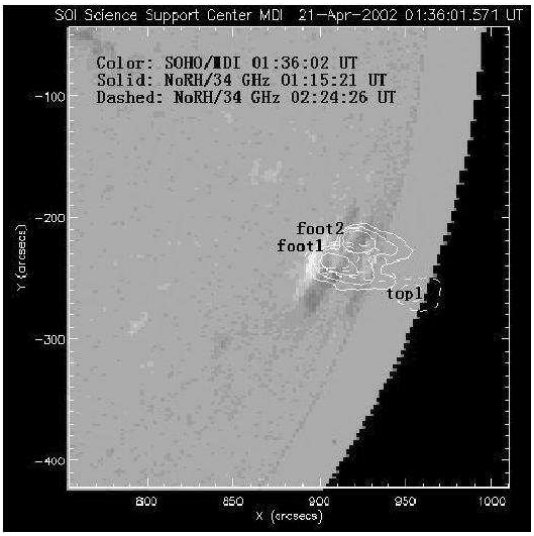

Fig. 20. The SOHO/MDI magnetograph overlaid by 34 GHz contours at 01:15:21 (solid) and 02:24:26 (dashed) UT

spectra of Hiraiso and Chinese Radio Spectrographs. There are a pair of moving type *IV* bursts respectively at 0.2-2 GHz from higher to lower frequencies and at 2.6-3.8 GHz from lower to higher frequencies (Fig.24).

The fine structures with fast frequency drifts evidently exist in the the type *IV* continuums at 0.2-2.0 GHz and 2.6-3.8 GHz. The dynamic spectra at 2.6-3.8 GHz with time resolution of 8 ms (Fig.25) are selected in four time intervals marked in Fig.24. The strong fluctuations at 2.6-3.8 GHz (Figs.22-23) indicate that the type *IV* bursts are not real continuums. A group of quasi-periodic emission clusters are shown in the top panel of Fig.25. There are very slow frequency drift of moving type *IV* (5 MHz/s) and the very fast drift of type *III* (several GHz/s) respectively in second and third panels. The fourth panel shows the multiple zebra strips with middle frequency drift (50 MHz/s). The three components of frequency drifts are

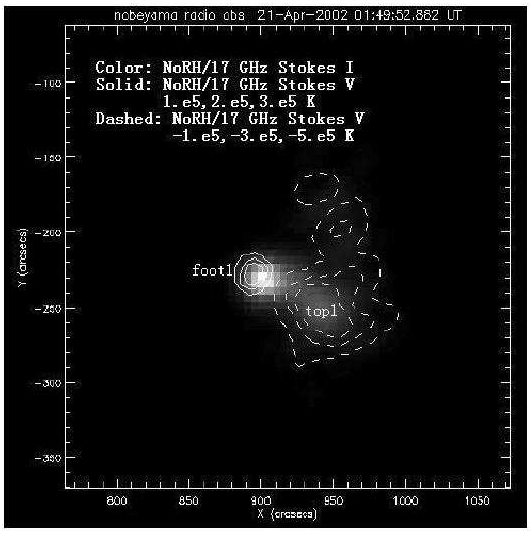

Fig. 21. The contours of Stokes V at 17 GHz are overlaid on Stokes I image at 17 GHz of NoRH (01:49:53 UT)

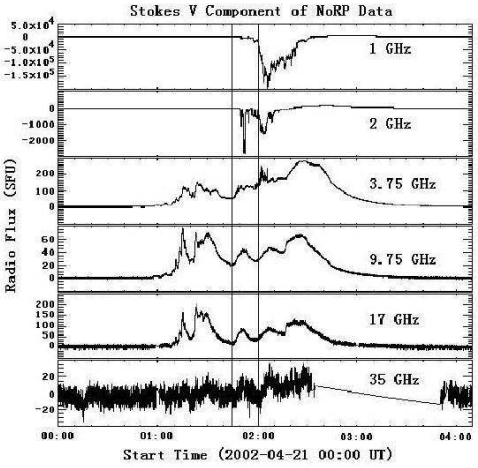

Fig. 23. The Stokes V profiles at 1, 2, 3.75, 9.75, 17 and 35 GHz of NoRP in the event

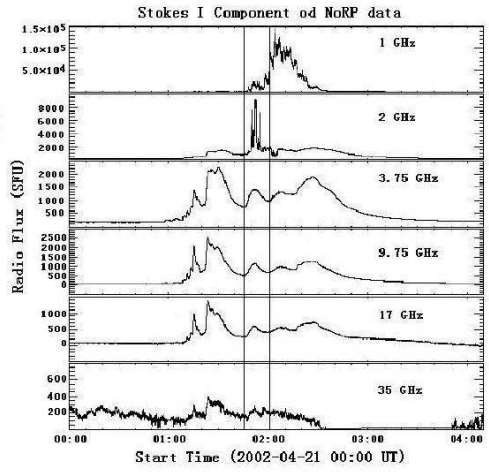

Fig. 22. The Stokes I profiles at 1, 2, 3.75, 9.75, 17 and 35 GHz of NoRP in the event

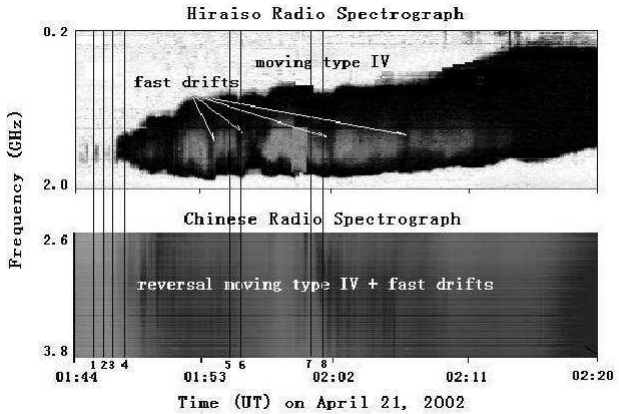

Fig. 24. A pair of moving type *IV* bursts at 0.2-2.0 GHz and 2.6-3.8 GHz

mixed in all panels of Fig.25., which may correspond to different speeds of current sheet or flare loop (tens km/s), shock waves (hundreds km/s), and non-thermal electrons (tens or hundreds keV) associated with magnetic reconnections that took place above the 17 GHz loop-top source in Figs.19-21.

The location of FS sources are also studied in some recent papers for zebra structures at 4.5-7.5 GHz with data of SSRT and Chinese spectrographs (Altyntsev et al., 2004; Melnikov et al., 2004).

4. Summary

The approximations of Dulk & Marsh may be used for diagnosis of coronal magnetic field and non-thermal electrons with non-thermal gyro-synchrotron radiations when

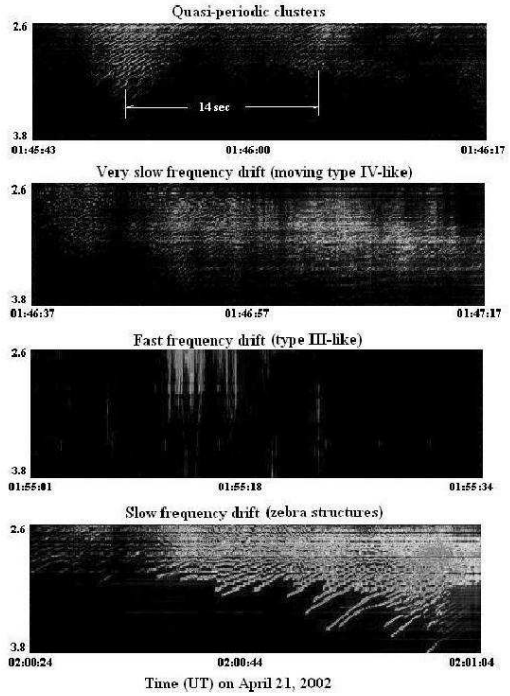

Fig. 25. The quasi-periodic emission clusters and three components of frequency drifts from top to bottom in the dynamic spectra at 2.6-3.8 GHz.

the low energy cutoff is close to 10 keV, as well as the other conditions given in Dulk & Marsh (1982) are satisfied. A series of papers (Zhou et al., 1994; Huang et al., 2000; 2002) are completed for this purpose, some explicit functions of coronal magnetic field and non-thermal electrons are derived from the self-consistent calculations with measurable values of frequency, turnover frequency, flux or brightness temperature, and spectral index.

On the other hand, if the low energy cutoff varies in a broad range (Gan et al., 2002), the coronal magnetic field and low energy cutoff should be calculated simultaneously with more strict model of non-thermal gyro-synchrotron radiations (Ramaty, 1969; Takakura et al., 1970). The other parameters are not sensitive to the calculations, such as the high energy cutoff, propagation angle, the density and temperature of ambient plasma (Huang et al, 2004c). Therefore, the new method will be developed for radio diagnosis coronal magnetic field and non-thermal electrons with non-thermal gyro-synchrotron radiations.

The another topic mentioned in this paper is the location of radio bursts with FS. Especially, the bursts or the FS with frequency drifts, such type *III* bursts and millisecond spikes with very fast drifts caused by particle accelerations, the moving type *IV* bursts with slow drifts caused the moving of flare and post-flare loops, or the middle drifts of the zebra structures caused by shock waves. The location of these bursts or FS may give some direct or indirect signature of magnetic reconnections and particle accelerations. The key point to locate the sources of the radio bursts with FS is how to joint the data of heliographs with high spatial resolution and the data of spectrographs with high temporal and frequency resolutions.

References

Altyntsev, A. T., Grechnev, V. V., Zubkova, G. N., Kardapolova, N. N., Lesovoi, S. V., Rosenraukh, Y. M., and Treskov, T. A., 1995, A&A, 303, 249
Altyntsev, A. T., Kuznetsov, A. A., Meshalkina, N. S., and Yan Yihua, 2004, A&A (accepted)
Bastian, T. S., 1994, ApJ, 426, 774
Benz, A. O., Jaeggi, M., and Zlobec, P., 1982, A&A, 109, 305
Benz, A. O., 1986, Solar Phys., 104, 99
Dulk, G. A., and Marsh, K. A., 1982, ApJ, 259, 350
Dulk, G. A., 1985, ARA&A, 23, 169
Forbes, T. G., 2004, Proceedings of IAU Symposium 226, (invited review)
Gan, W. Q., Li, Y. P., and Zhang, J., 2001, ApJ, 552, 858
Huang, G. L., 1987, Solar Phys., 114, 363
Huang, G. L., Qin, Z. H., Yang, G., Fu, Q. J., and Liu, Y. Y., 1998, ApSS, 259, 317
Huang, G. L., and Zhou, A. H., 1999, New Astron., 4, 591
Huang, G. L., and Nakajima, H. 2002, New Astron., 7, 135
Huang, G. L., Wu, H. A., Grechnev, V. V., Sych, R. A., and Altyntsev, A. T., 2003, Solar Phys., 213, 341
Huang, G. L., 2004a, JGR, 109, 2105
Huang, G. L., 2004b, A&A (accepted)
Huang, G. L., Zhou, A. H., Su, Y. N., and Zhang, J., 2004c, New Astron. (in press)
Huang, G. L., 2004d, ApSS (in press)
Huang, G. L., and Lin, J., Proceedings of IAU Symposium 226 (accepted)
Krüger, A., 1979, Introduction to Solar Radio Astronomy and Radio Physics, Reidel
Krucker, S., Aschwanden, M. J., Bastian, T. S., and Benz, A. O., 1995, A&A, 302, 551
Krucker, S., Benz, A. O., and Aschwanden, M. J., 1997, A&A, 317, 569
Kundu, M. R., 1990, Mem. S.A.It., 61, 431.
Kundu, M. R., Garaimov, V. I., White, S. M., and Krucker, S., 2004, ApJ, 600, 1052
Liu, Y.Y., Fu, Q.J., Qin, Z.H., Huang, G.L., and Wang, M., Science in China (Series A), 45, 114
Mclean, D. J., ed., 1985, Solar Radio Physics, Cambridge Press
Melnikov, V. F. et al., 2004 (to be submitted)
Robinson, P. A., and Benz, A. O., 2000, Solar Phys., 194, 345
Ramaty, R., 1969, ApJ, 158, 753
Takakura, T., and Scalise, E., 1970, Solar Phys., 11, 434
Xie, R. X., Fu, Q. J., Wang, M., and Liu, Y. Y., 2000, Solar Phys., 197, 375
Zhou, A. H., & Karlický, M., 1994, Solar Phys., 153, 441
Zhou, A. H., and Su, Y. N., 2004, Solar Phys. (accepted)